(Received 9 December 2024, Accepted 30 December 2024, Scheduled 9 January 2025)

Wideband High Gain Lens Antenna Based on Deep Learning Assisted Near-Zero Refractive Index Metamaterial

Huanran Qiu[1, 2, †], Liang Fang[3, †], Rui Xi[1, 2, 4, *, †], Yajie Mu[2], Dexiao Xia[2], Yuanhao Zhang[1], Shiyun Ma[1], Jiaqi Han[2], Qiang Feng[2], Ying Li[5, 6, 7], Hong Xu[1, 4], Bin Zheng[5, 6, 7, *], and Long Li[2, *]

[1] *Hangzhou Institute of Technology, Xidian University, Hangzhou 311231, China*
[2] *Key Laboratory of High-Speed Circuit Design and EMC of Ministry of Education School of Electronic Engineering, Xidian University, Xi'an 710071, China*
[3] *The Research Institute for Special Structures of Aeronautical Composite AVIC Innovation Center for Electromagnetic Functional Structure, Jinan 250023, China*
[4] *National Key Laboratory of Radar Signal Processing, Xidian University, Xi'an 710071, China*
[5] *State Key Laboratory of Extreme Photonics and Instrumentation ZJU-Hangzhou Global Scientific and Technological Innovation Center, Zhejiang University, Hangzhou 310027, China*
[6] *International Joint Innovation Center The Electromagnetics Academy at Zhejiang University, Zhejiang University, Haining 314400, China*
[7] *Jinhua Institute of Zhejiang University, Zhejiang University, Jinhua 321099, China*

ABSTRACT: Deep learning neural network (DLNN) has enormous potential in solving electromagnetic inverse design problem, and thus meet the growing demand for rapid high gain antenna design in current industrial applications and other complex questions. Here, we propose a wideband near-zero refractive index high gain antenna based on dual band near zero refractive index frequency selective surface (DB-NZRI FSS) with the aid of Fourier transform neural network (FTNN). FTNN employs a Fourier transform-based data simplification algorithm to address the prevalent issue of long training time in neural network for antenna design. We verify the universal adaptive and effectiveness of FTNN by rapid designing near-zero refractive index metamaterial working in adjacent bands. The proposed DB-NZRI FSS unit has transmission zeros at the magnetic resonance point and electric resonance point, and a stopband with high reflectivity exists between the two points. By integrating the initial highly directional radiation effect of zero refractive index metamaterial with the planar parallel cavity principle, the proposed lens antenna obtains the maximum gain of 12.64 dBi at 8.2 GHz. The FTNN has high accuracy and low loss of 0.0407. The designed DB-NZRI FSS has relatively low profile of 3 mm (8% wavelength at the central frequency of 8.2 GHz). Besides, the designed antenna has the characteristics of dual polarizations and wideband with the relative 3 dB gain bandwidth of 19.35% (7.56–9.18 GHz).

1. INTRODUCTION

In recent years, metamaterials have been extensively explored due to its distinctive features that do not exist in nature, such as left handed material [1, 2] chromatic aberration-free metamirrors [3], superscattering [4], invisibility cloaking [5–12], illusion devices [13], topological insulator [14], beam deflection [15, 16], beam focusing [17], high gain [18–21], orbital angular momentum vortex beams generation [22–24], and multibeam antenna [25–28]. Previously, metamaterials with unique function were designed purposely by following some physical and mathematical guiding rules, which belong to the paradigm of forward design. For example, when designing high gain metamaterial antenna, the equivalent circuit method is often utilized to guide the parameters optimization of the metamaterials [29]. Phase gradient across the metamaterial aperture is constructed to achieve antenna beam deflection [30]. To quickly and efficiently complete the design of metamaterial antennas, recent research has proposed the deep learning neural network (DLNN) [31] to inverse design metamaterial structures [32–34].

DLNN has been widely applied to tasks such as logic operations [35], data analysis [36], pattern recognition [37], intelligent control [38, 39], and predictive modeling [40]. By analyzing and mining large-scale data with deep learning models, hidden patterns and trends from the data can be quickly and effectively extracted, deepening our understanding of complex systems. DLNN has shown great potential in solving electromagnetic inverse problems of rapid industrial design. This enables the quick and cost-effective design of high-gain antennas or the improvement of existing antenna performance.

Traditional inverse design methods, such as genetic algorithm [41], adjoint method [42], and boundary element method [43], usually require manual analysis of data to obtain several key input points of the neural network. It is time consuming and may result in key points missing. On the other hand, if the complete data curve is utilized as the input data, extended training time and increased computing resources are

* Corresponding authors: Rui Xi (xirui@xidian.edu.cn); Bin Zheng (zhengbin@ zju.edu.cn); Long Li (lilong@mail.xidian.edu.cn).
† Huanran Qiu, Liang Fang, and Rui Xi contributed equally to this work.

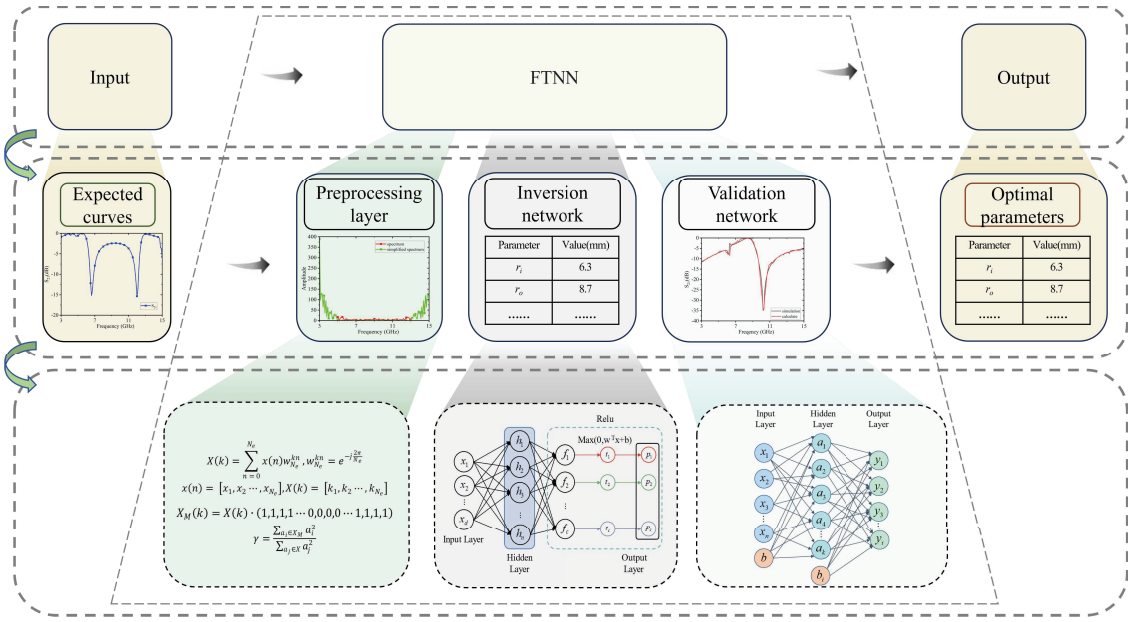

FIGURE 1. Schematic diagram of the hybrid architecture of the proposed FTNN.

inevitable. Previous studies have found that the correspondence between function and metamaterial structure is usually not a deterministic one-to-one problem, but a one-to-many multi-value problem [44]. Therefore, it is necessary to cascade a validation network after the inverse design network to verify whether the calculation results are correct.

In order to solve this problem, we proposed Fourier transform neural network (FTNN), a tandem neural network (TNN) with simplified algorithm based on Fourier transform. We take the complete simulation S parameter curve data as input, and the FTNN can then process the data by reducing data volume to half or even smaller. Therefore, there is no need for manual selection of key points, and the demand for computing resources is reduced.

In addition, TNN is utilized due to the simplification of the original one to multivalued problem of inverse design into a one-to-one single valued problem, which is achieved by validating the output results and calculating the expected error based on a validation network [45]. For the specific construction of FTNN, we use PyTorch framework to assist in building the whole neural network hybrid architecture. Meanwhile, due to the involvement of complex data in the simplified data, we have made improvements to the forward propagation process and loss calculation function, enabling the neural network to effectively handle complex data.

Previous research has explored complex activation functions, including modReLU, zReLU, and CReLU activations [46]. Our FTNN adopts the CReLU activation function, which activates the real and imaginary parts respectively.

The proposed FTNN, illustrated as a hybrid architecture in Fig. 1, has three modules that include a Fourier transform-based data preprocessing algorithm served as the preprocessing layer, a complex inverse design neural network served as the inversion network, and a complex forward design neural network served as the validation network.

To verify the effectiveness and applicability of the FTNN, we used it to assist the design of a wideband near-zero refractive index metamaterial and obtain a high gain antenna based on the metamaterial.

A near-zero refractive index frequency selective surface (NZRI FSS) is an artificial material surface that has a unique refractive index close to or exactly zero [47–49]. According to Snell's law, the refractive angle transmitted through the NZRI FSS always approaches vertical to the zero refractive surface even if the incident angle is large, which is different from traditional materials. The dual band near zero refractive index frequency selective surface (DB-NZRI FSS) proposed in this article has near zero refractive index points in two bands, which are also the transmission poles with the highest transmission. There is a high-reflection band between two near zero refractive index points. So according to the principle of planar parallel cavity [50], the proposed DB-NZRI FSS will experience constructive interference of electromagnetic waves while working in the high-reflection band after loading the antenna, which will ultimately achieve an enhanced antenna gain.

Previous studies have shown the widespread application of NZRI FSS metamaterials in various fields, such as frequency conversion [51, 52], broadband absorber [53], and high gain antenna [47–49]. However, most of these studies focus on obtaining zero refractive index based on near-zero permittivity, and significant effort has been spent on optimizing and modifying model structures. This paper proposes a high gain antenna constructed with DB-NZRI FSS and the aid of DL. Compared to previous studies, the proposed DB-NZRI FSS achieves zero refractive index characteristic through both near-zero permittivity and near-zero permeability, with the aid of Fourier transform to significantly accelerate the model design process.

This paper proposes a high gain antenna constructed with FTNN optimized DB-NZRI FSS. Compared with previous studies, the proposed DB-NZRI FSS achieves dual-band zero refractive index characteristic through both near-zero permittivity and near-zero permeability, and the simplified FTNN algorithm is proposed to significantly accelerate the model design process. Specifically, this article utilizes the high reflection characteristics of the DB-NZRI FSS, and an electromagnetic bandgap structure is constructed by cascading multiple layers of DB-NZRI FSS, with near-zero refractive bands of each layer working in adjacent bands. According to the principle of plane parallel cavity, this structure allows electromagnetic waves to reflect multiple times between the antenna ground plane and multilayer cascaded DB-NZRI FSS, realizing constructive interference to achieve high gain emission. In addition, by utilizing the vertical emission characteristics of DB-NZRI FSS, the beam propagating in other directions is redirected to the normal direction of DB-NZRI FSS, further enhancing the gain as shown in Fig. 2.

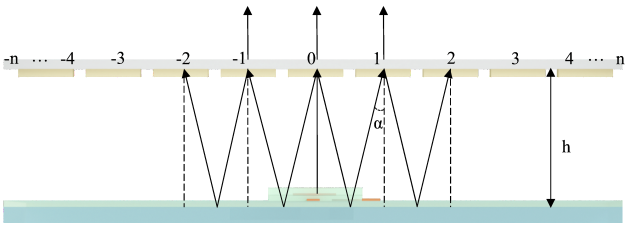

FIGURE 2. The schematic diagram of multiple reflections and deflection of electromagnetic waves.

In addition, this article proposes a fast inverse design network algorithm based on Fourier transform transform neural network (FTNN) and utilizes it to assist DB-NZRI FSS design. By combining efficient deep learning algorithms with traditional design methods, an efficient design of near-zero refractive metamaterial is thus successfully achieved. Fig. 1 and Fig. 3 show schematic diagram of the proposed FTNN process and schematic diagram of wideband high gain antenna based on DB-NZRI FSS. Compared with using HFSS to sweep the parameters and manually optimize, FTNN only needs less than 2 minutes of training time to give the corresponding model parameters, which greatly accelerates the design speed.

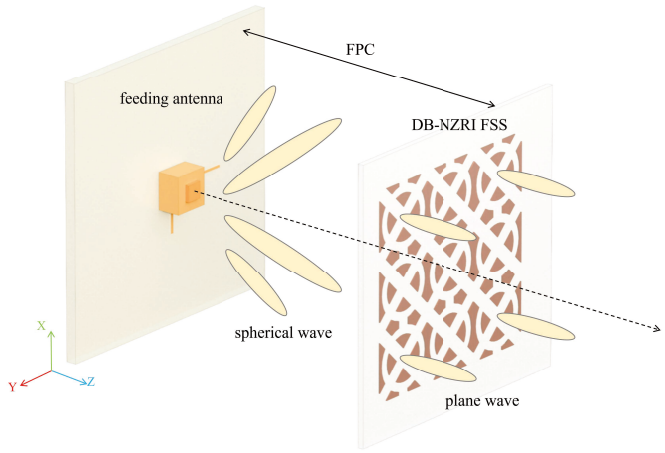

FIGURE 3. Schematic diagram of wideband high gain antenna based on DB-NZRI FSS.

2. STRUCTURE AND METHODOLOGY

2.1. Design of Wideband Near-Zero Refractive Index Metamaterial

As shown in Fig. 4, the DB-NZRI FSS is composed of a single-layer unit, which consists of a substrate with metal patterns printed on both sides. The square substrate is F4B dielectric with a dielectric constant of 2.65. The substrate has a side length of l_1 and thickness h.

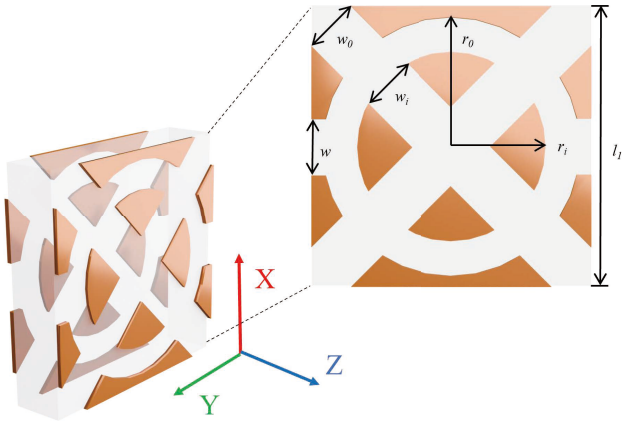

FIGURE 4. Structure of the DB-NZRI FSS unit.

The metal pattern features a complementary dual-layer symmetric resonant ring structure, which is composed of a square patch etched with a circle slot and multiple rectangular slots. The inner and outer radii of the circle slot are r_i and r_o, respectively. The orthogonal rectangular slots within the inner ring have a width of w_i; the orthogonal rectangular slots in the outer ring have a width of w_o; and the rectangular slot along the y-axis has a width of w. Specific structural parameters are listed in Table 1.

TABLE 1. Structural parameters of the DB-NZRI FSS initial unit.

Parameter	Value (mm)	Parameter	Value (mm)
r_i	6.3	w_o	4
r_o	8.7	w_i	3
l_1	18	w	3
h	3	/	/

The structure is a combination of electric and magnetic resonant components. The two arms along the x-axis form an electric resonant arm. Together with the two arms along the y-axis, a capacitor is created with a width of w_o, producing electric resonance. The gaps in the y-axis arms act as openings in the resonant ring, enabling electric coupling and magnetic resonance.

We extracted and analyzed the constitutive parameters of the DB-NZRI FSS unit using the method described in [54]. Define the incident wave as being normally incident on the unit. The electric field is applied along the y-axis. The transmission characteristics of the unit are shown in Fig. 5.

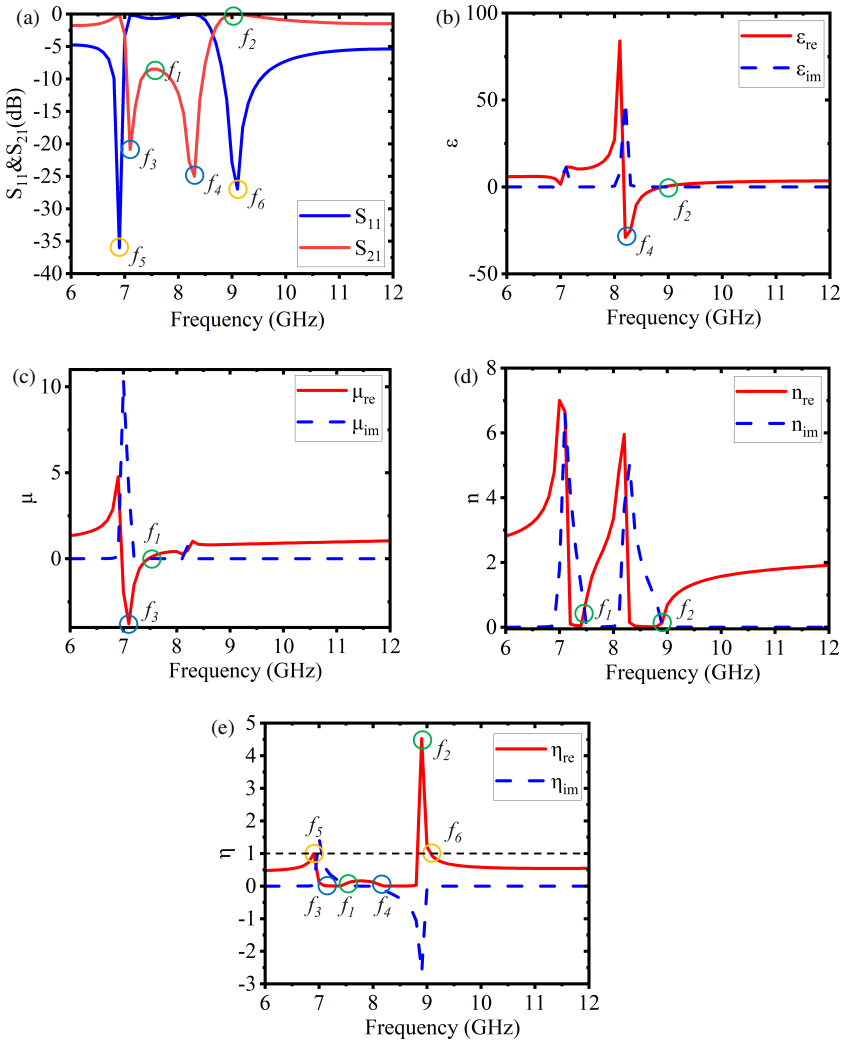

FIGURE 5. Characteristics of the single-layer zero-index metamaterial unit. (a) S_{11} and S_{21}, (b) permittivity, (c) permeability, (d) refracture index, (e) normalized wave impedance.

As shown in Fig. 5, the unit exhibits near-zero magnetic permeability and near-zero refractive index characteristics at $f_1 = 7.5$ GHz, near-zero electric permittivity and near-zero refractive index characteristics at $f_2 = 9$ GHz. The unit displays strong magnetic resonance at $f_3 = 7.1$ GHz and strong electric resonance at $f_4 = 8.2$ GHz. Based on the S-parameters, it is evident that the unit has two transmission zeros at 7.1 GHz and 8.2 GHz, corresponding to the strong magnetic resonance at f_3 and strong electric resonance at f_4, respectively. Transmission poles occur at $f_5 = 6.9$ GHz and $f_6 = 9$ GHz, and the latter corresponds to the electric resonance point f_2. The band-stop characteristic of the proposed DB-NZRI FSS is observed in Fig. 5(a), and there is a stopband with high reflection between the two strong resonance frequencies f_3, f_4. According to the principle of planar parallel cavity, this structure allows electromagnetic waves to achieve multiple reflections between the antenna ground plane and DB-NZRI FSS for high gain achievement.

As illustrated in Fig. 6, the electric field distribution in the yoz plane of the TEM waveguide model at various resonance frequencies reveals that the unit transmits most of the electric field at the electric near-zero-point f_2. In contrast, at the magnetic near-zero-point f_1 and the two transmission zeros, only a small amount of the electric field passes through. This is due to changes in the dielectric constant and permeability causing variations in the normalized wave impedance. The normalized wave impedance at f_1 and f_2 is zero and at its peak, respectively, while at the transmission zeros f_3 and f_4, the normalized wave impedance is approximately zero, mismatching with air. At the transmission pole f_5, the normalized wave impedance is 1, matching well with air. Although there is an impedance mismatch at f_2, the electric permittivity is zero at this point, resulting in an ENZ (epsilon-near-zero) tunneling effect, thus achieving excellent transmission performance.

2.2. Proposed Fourier Transform Neural Network (FTNN)

The process of the proposed FTNN-assisted metamaterial unit optimization design is as follows: Firstly, a desired result curve (e.g., S_{21} curve) is plotted and used as the input to the neural network; next, the preprocessing layer will use the FFT simpli-

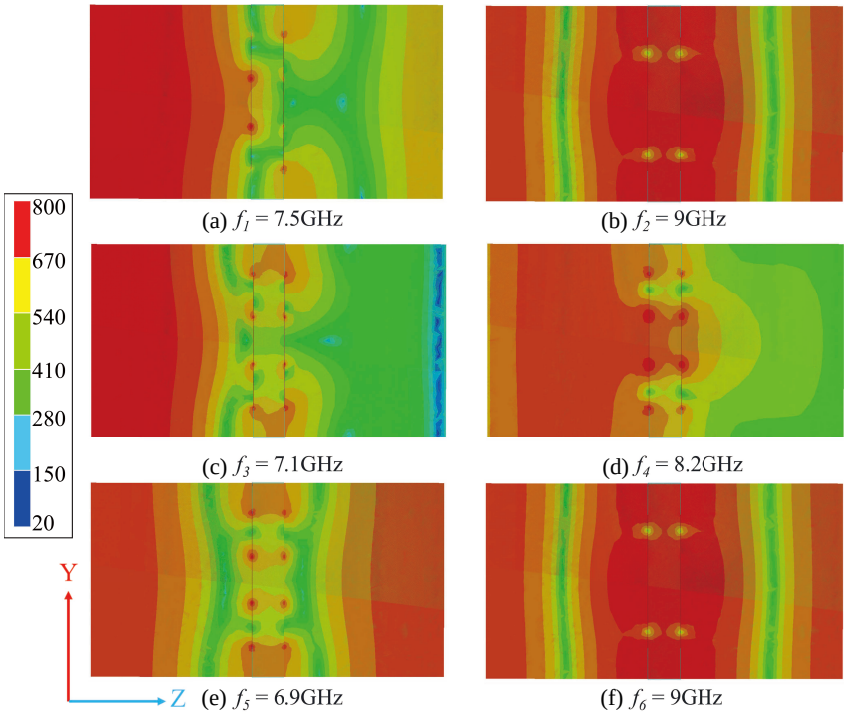

FIGURE 6. Electric field distribution at each resonance points on the YOZ plane of the TEM waveguide unit. (a), (b) at magnetic near zero-point f_1 and electric near zero frequency point f_2, (c), (d) at transmission zero-point f_3 and f_4, (e), (f) at transmission pole f_5 and f_6.

fication algorithm to simplify the input data into complex data, and after this step, the number of input data points can be effectively reduced to half of the original data points or lower with almost no loss of information; after that, the inversion network will use the simplified data to predict the corresponding structural parameters and pass the result to the validation network; the validation network will use the predicted structural parameters to calculate the corresponding simplified data or S_{21} curve, and the loss of FTNN can be obtained by comparing the two simplified data; if the error is low enough (lower than 0.1), it can be considered as valid. The predicted structural parameters of FTNN can be used to guide the design of the metamaterial.

We conducted a performance comparison between the TNN and FTNN when facing the same inverse design task. In order to clearly understand the improvement of FTNN compared to the TNN. We have chosen mean errors as performance indicator. In each model, we used the same setting for hyperparameters to ensure the fairness of comparison.

As shown in Fig. 7, FTNN has higher computational accuracy than TNN. Next, it is necessary to analyze and introduce the FFT simplification algorithm we used. Inspired by data preprocessing method in digital signal processing, the system first uses Equation (1) and Equation (2) to simplify the input data volume with a Fourier transform [55]. $x(n)$ represents the input data; $X(k)$ represents the transformed spectrum; N_e represents the number of points in the input data; n and k represent the n^{th} and k^{th} points in the curve and spectrum.

$$X(k) = \sum_{n=0}^{N_e} x(n) w_{N_e}^{kn},\ w_{N_e}^{kn} = e^{-j\frac{2\pi}{N_e}} \tag{1}$$

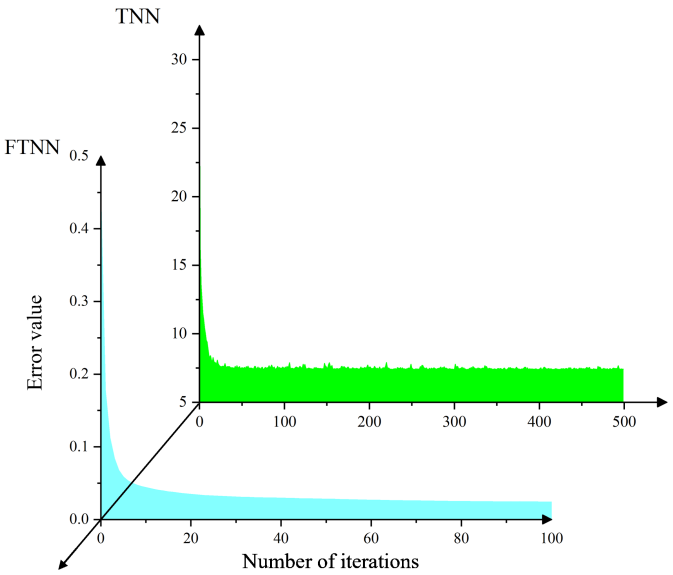

FIGURE 7. The comparison between TNN and FTNN.

$$x(n) = [x_1, x_2, \cdots, x_{N_e}],\ X(k) = [k_1, k_2, \cdots, k_{N_e}] \tag{2}$$

The input and output of the FFT simplification algorithm are shown in Fig. 8. We can see from Fig. 8 that the input is an S_{21} curve, and its spectrum is obtained after FFT transformation. Analyzing its spectrum reveals that the values in the spectrum are concentrated at both ends. Since the value of the spectrum can reflect the energy level of the frequency points [55], a low-pass filter can be used to remove the middle to high frequency components and only retain the low-frequency compo-

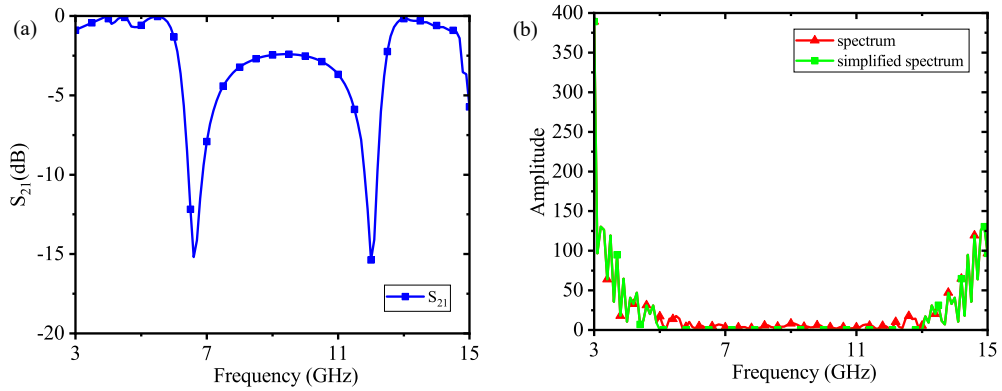

FIGURE 8. Using FFT to obtain spectrum and simplified spectrum. (a) S_{21} curve, (b) spectrum and simplified spectrum.

nents at both ends, thus preserving the sampling point without losing too much information. The simplified formula is shown in Equation (3), where $X_m(k)$ represents the simplified spectrum, $X(k)$ the spectrum, and k the k^{th} point in the spectrum.

$$X_m(k) = X(k) \cdot (1, 1, 1, 1, ...0, 0, 0, 0...1, 1, 1, 1) \quad (3)$$

We calculate the energy proportion of the simplified results using Equation (4). In Equation (4), a_j and a_i represent the j^{th} and i^{th} points in the spectrum and simplified spectrum; X and X_M represent the spectrum and simplified spectrum; γ represents the energy proportion of the simplified spectrum to the total spectrum.

$$\gamma = \frac{\sum_{a_i \in X_M} a_i^2}{\sum_{a_j \in X} a_j^2} \quad (4)$$

Generally, it can be considered that the Fourier series subspace inherits enough information to meet the FTNN training requirements when $\gamma > 0.95$. The N_e-dimensional data with only real part is thus reduced to $2M$-dimensional complex data, and thus the data volume simplification is realized. The simplified data can then be transmitted to the complex inverse neural network for training.

The neural network framework provided by PyTorch can only handle real numbers. Therefore, when being faced with input complex data, its real and imaginary parts can only be separated into two sets of real data inputs. This will result in the loss of correlation information contained between the real and imaginary parts of complex data.

To address this issue, we have improved the PyTorch framework and made modifications including but not limited to the forward propagation process and loss calculation part. A complex data neural network is then proposed, capable of performing activation and other operations on input complex data.

The data input part of the complex inverse neural network uses DataLoader in Pytorch for convenient dataset composition, single-thread or multi-thread reading, batch size settings, data shuffling, and placing data on the GPU.

The complex inverse neural network uses the Adam adaptive learning rate optimizer with L2 regularization. The adaptive learning rate optimizer effectively suppresses gradient explosion and vanishing gradient issues, reducing the time needed to find a suitable learning rate. L2 regularization constrains the model's parameters by introducing an additional penalty term in the loss function, thereby reducing the model's complexity. This additional penalty is related to the magnitude or number of the model's parameters and aims to encourage the model to learn simple patterns rather than overfitting the training data. Consequently, it effectively reduces the model's complexity, lowers the risk of overfitting, and controls the variation in weight values, thereby preventing gradient explosion.

To calculate input complex data, the linear operations during each forward propagation are changed to complex multiplication, as shown in Equation (5), where $W = A + iB$ is the parameters of complex neural networks; $h = x + iy$ is the input complex data; and $W * h$ is the forward propagation process of FTNN.

$$W * h = (A * x - B * y) + i(B * x + A * y) \quad (5)$$

The loss function of the model uses a modified MSELoss function, as shown in Equation (6), which calculates the sum of the squared differences between the predicted and true values' real and imaginary parts, where a is the predicted simplified spectrum; b is the input simplified spectrum; E_{loss} is the deviation between FTNN output and expected output.

$$\begin{aligned} E_{\text{loss}} &= \text{loss}(a, b) \\ &= (\text{Re}(a) - \text{Re}(b))^2 + (\text{Im}(a) - \text{Im}(b))^2 \end{aligned} \quad (6)$$

The training progress of the neural network is controlled by setting an iteration limit and a stopping mechanism. If the loss function value E_{loss} meets the set threshold and remains stable for 50 epochs or reaches the maximum number of iterations, training ends. Otherwise, the structure (the number of hidden layers) and hyperparameters (learning rate, weight) of neural network are adjusted, and training is resumed. The performance of FTNN is evaluated using the loss function Equation (6) to find the hyperparameters that minimize the loss function, resulting in the desired FTNN.

Based on the traditional inversion network, a set of S-parameter curves always correspond to multiple sets of structural parameters, which results in a non-convex (multivalued issue) problem. A forward neural network after the inversion network is then added here to transform the nonconvex problem to a convex (single valued issue) problem, improving model reliability [44].

Finally, a forward design neural network constructed as a validation network is cascaded at the output end of the inversion network. The structure of the validation network is similar to that of the inverse neural network, but the input-output is opposite.

The validation network is built on the PyTorch framework, utilizing a fully connected architecture with early stopping and random data input mechanisms. The neural network uses the adaptive Adam optimizer with L2 regularization. The activation function used is the CReLU function, which facilitates efficient gradient descent and backpropagation while avoiding gradient explosion and vanishing gradient issues. The loss function of the model is the modified MSELoss function, averaging the squared differences between predicted and true values. The designed FTNN neural network can inversely predict the structure parameters of the DB-NZRI FSS unit using ideal S parameter curve as input. As the FTNN neural network is based on a data-driven model, we need to prepare enough datasets before training the network. Therefore, we utilized the widely used commercial full wave simulation software HFSS to generate S_{21} data. The training dataset was collected by uniformly sampling the metamaterial parameters.

The unit thickness was set at 1 mm, which is ultra-thin $(1/36.6\lambda)$ at center working frequency of 8.2 GHz. The key parameters affecting the near-zero refractive frequency positions are widths w_o and w_i, which are concluded from parameter analysis. They are thus used as the output of FTNN, and the ideal S_{21} data are used as input for FTNN. We first need to train the validation network part of FTNN. The FTNN is trained using 444 sets of S_{21} data generated by HFSS full-wave simulation, with 400 sets used as the training set and the remaining 44 sets as the validation set. The training time is 35.01 seconds, while the training loss is 0.0153, and the validation loss is 0.0147, demonstrating high accuracy.

Verify the accuracy of the validation network by randomly selecting the structural parameters $X_1 = [w_o, w_i] = [2.6, 0.85]$ within the training set and $X_2 = [w_o, w_i] = [3.2, 3.2]$ outside the training set. They are input into the validation network and output the predicted S-parameter curve, which is then compared with the full wave simulation curves of HFSS. If the prediction curve of the validation network is consistent or similar to the full wave simulation S curve of HFSS, it can be considered that the validation network can accurately predict the full wave simulation curve. This demonstrates the ability of validation network to replace full wave simulation and quickly obtain full wave simulation curves.

The comparison between the validation network predicted curves and HFSS full-wave simulation curves is shown in Fig. 9.

As shown in Fig. 9, the simulation S data results closely match the predicted output of FTNN. This indicates the accuracy of the proposed validation neural network and demonstrates its potential to replace simulation software for fast simulation.

Next, it is necessary to test FTNN. Considering that each set of S_{21} data has 121 points, $M = 25$ is chosen to establish the Fourier transform subspace, compressing the 121 points to 50

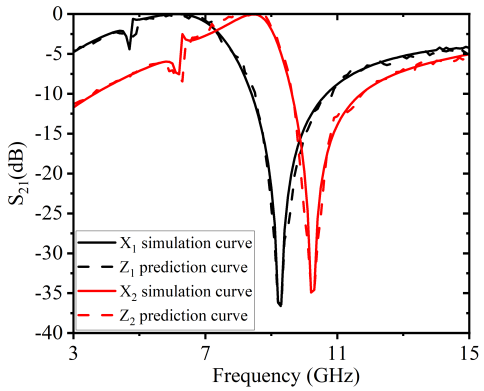

FIGURE 9. Comparison between prediction curves and simulation results, within the training range and outside the training range.

points, with approximately 0.98 (meeting the requirement $>$ 0.95). The model's training time is 1.145 minutes; the training loss is 0.029; and the validation loss is 0.0407, demonstrating high accuracy.

With the key structure parameters, $X_1 = [w_o, w_i]$ set as $[2.6, 0.85]$ (which is within the training set), the related full-wave simulation S_{21} curve is then input into the FTNN. Compare the calculated results to verify whether the network has correctly and sufficiently learned the mapping relationship between the full-wave simulation response curve and structural parameters. With the key structure parameters $X_2 = [w_o, w_i]$ set as $[3.2, 3.2]$ (which is outside the training set), the related full-wave simulation S_{21} curve is then input into the FTNN. Compare the calculated results to verify whether the network has an overfitting problem.

The corresponding outputs of FTNN are $Z_1 = [w_o, w_i] = [2.5452, 0.8142]$ and $Z_2 = [w_o, w_i] = [3.1229, 3.1795]$, correctly predicting the corresponding structural parameters of the input full-wave simulation curves. This indicates that the FTNN has correctly learned the mapping relationship between the response curves and structural parameters and can effectively assist in subsequent antenna design.

Then, use the previously proposed DB-NZRI FSS unit as unit 1 and use FTNN to assist in designing unit 2, unit 3. The expected S_{21} curves of unit 2 and unit 3 are plotted as shown in Fig. 10. After inputting the curve into FTNN, we get that the values of w_o for unit 2 and unit 3 are 1.9264 and 0.6476, respectively, and the values of w_i are 1.5017 and 2.0373, respectively. The comparison of the expected curves and predicted curves is shown in Fig. 11.

Finally, considering manufacturing process factors, the structural parameters for unit 1, unit 2, and unit 3 are $w_o = 4, 2, 0.6$ and $w_i = 3, 1.5, 2$, respectively. The waveguide transmission method was used to simulate the transmission characteristics in HFSS, and the refractive index was calculated using MATLAB. The corresponding refractive index of DB-NZRI FSS unit is shown in Fig. 12, in which zero refractive index characteristics around $f_1 = 4.4$ GHz, $f_1' = 5.4$ GHz, $f_1'' = 7$ GHz, $f_2 = 8.4$ GHz, $f_2' = 8.6$ GHz, and $f_2'' = 10$ GHz are observed respectively. In order to better characterize the properties of the proposed near-zero metamaterials, in Fig. 13 the permittivity, permeability, refractive index, and effective impedance of

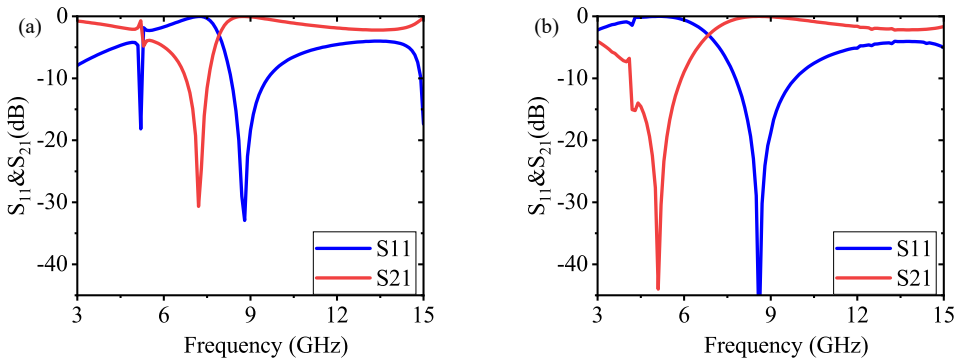

FIGURE 10. Expected curves used as input for FTNN to calculate the structural parameters of unit 2 and unit 3, (a) unit 2, (b) unit 3.

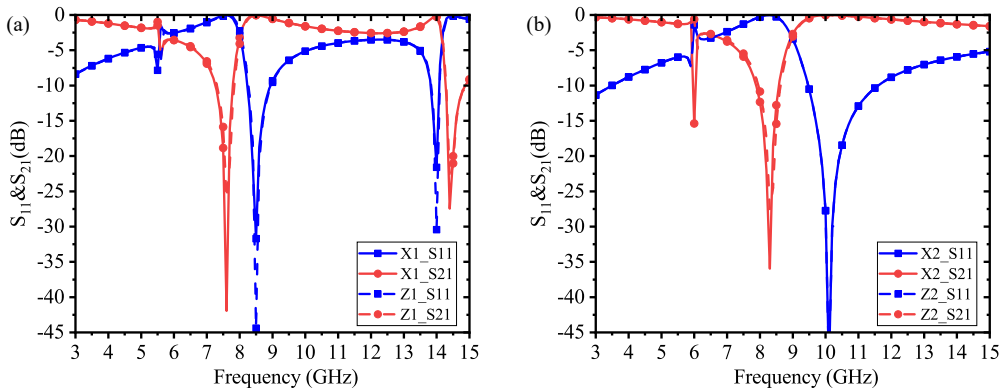

FIGURE 11. The comparison between the S_{21} curve of the prediction unit and the expected curve, (a) within the training set, (b) outside the training set.

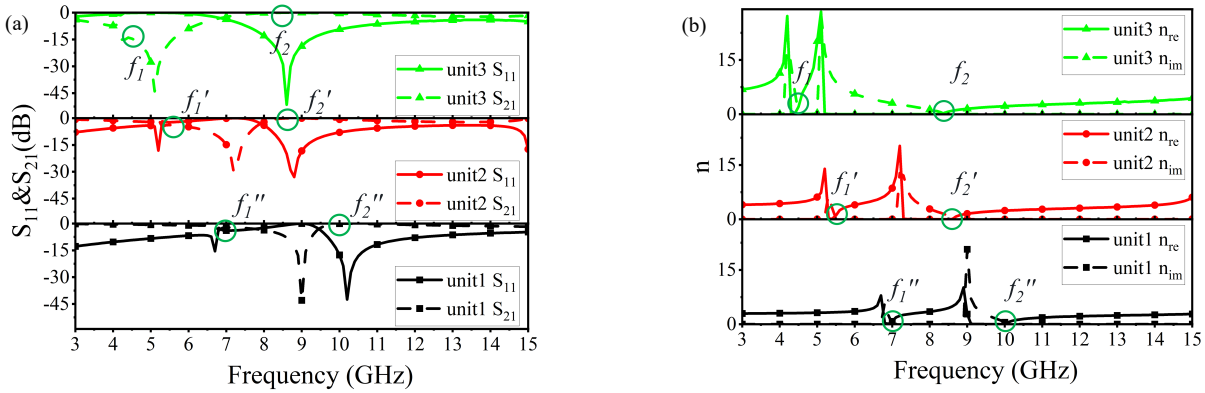

FIGURE 12. Characteristics and refractive index of unit 1, unit 2 and unit 3, (a) S_{11} and S_{21}, (b) refractive index.

unit 1, unit 2, unit 3 are plotted. Three units are cascaded with inter-layer distance set as 0 mm, which can further improve the bandwidth and gain of the antenna. This shows that the FTNN successfully achieves the inverse design goal.

3. HIGAN GAIN LENS ANTENNA BASED ON DB-NZRI-FSS

3.1. The Simulation Verification of High-Gain Antenna Based on DB-NZRI FSS

The wideband near-zero refractive index high gain antenna proposed in this article consists of a DB-NZRI FSS and a feed antenna. The feed antenna adopts a patch antenna with an L-shaped slot [56], and the specific design dimension has been explained in Fig. 14 and Table 2.

The previously designed DB-NZRI FSS unit is periodically arranged as a $3 * 3$ array and loaded on top of a patch antenna. The simulation analyses of its gain and electric field are compared, and the simulation results are shown in Fig. 15 and Fig. 16.

After loading a single-layer DB-NZRI FSS, the radiation field of the antenna is significantly improved from a spherical wave to a plane wave due to the vertical emission characteristics and planar parallel cavity principle. Comparing the gain

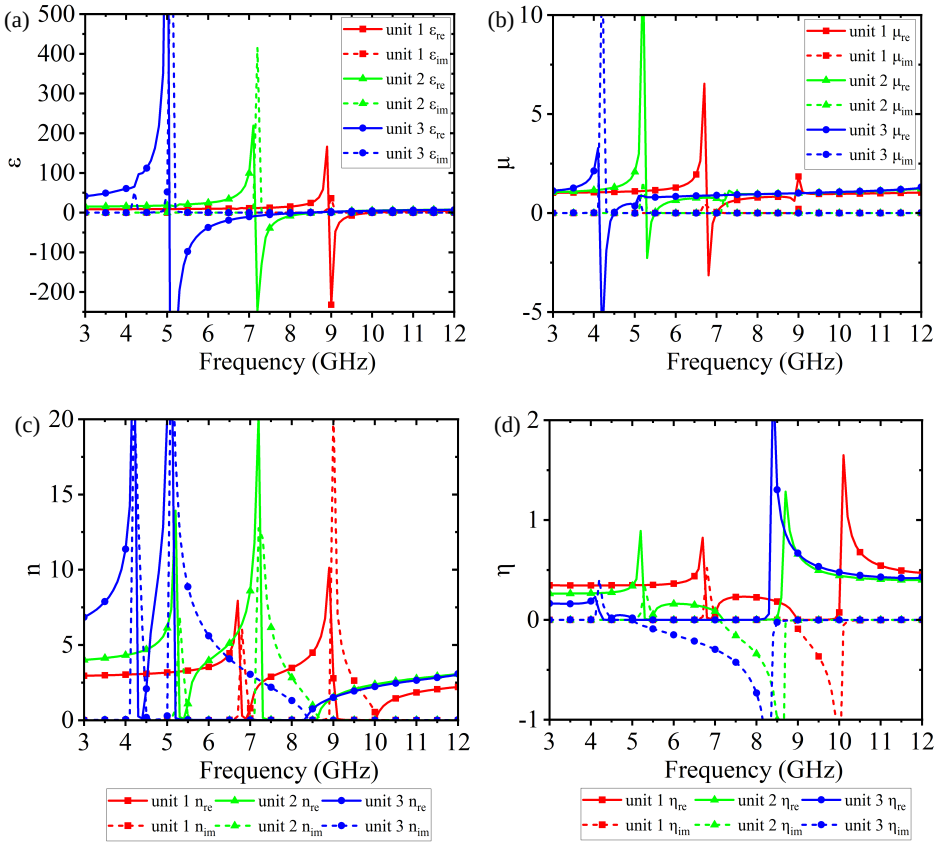

FIGURE 13. The permittivity, permeability, refractive index, and effective impedance of the three units, (a) permittivity, (b) permeability, (c) refractive index, (d) effective impedance.

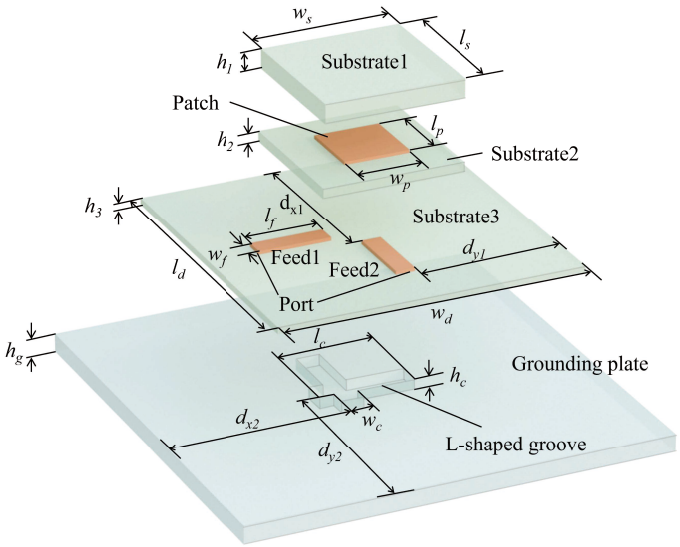

FIGURE 14. Structure of the feed antenna.

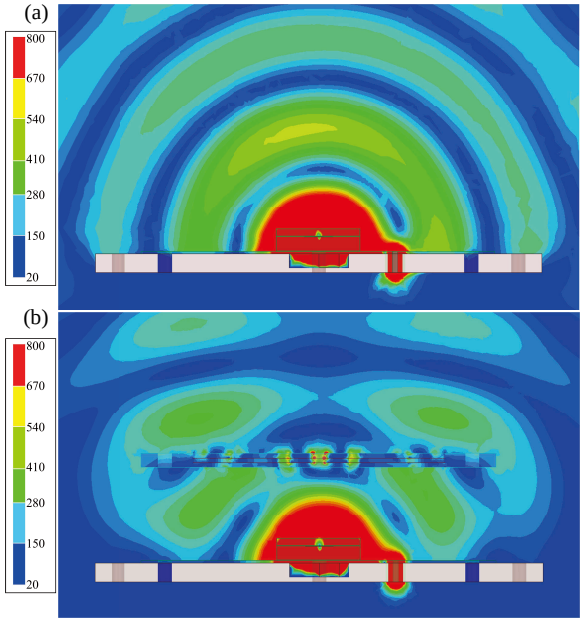

FIGURE 15. Comparison of electric field radiation, (a) electric field radiation pattern of feed antenna at 8.2 GHz, (b) electric field radiation pattern of metamaterial antenna at 8.2 GHz.

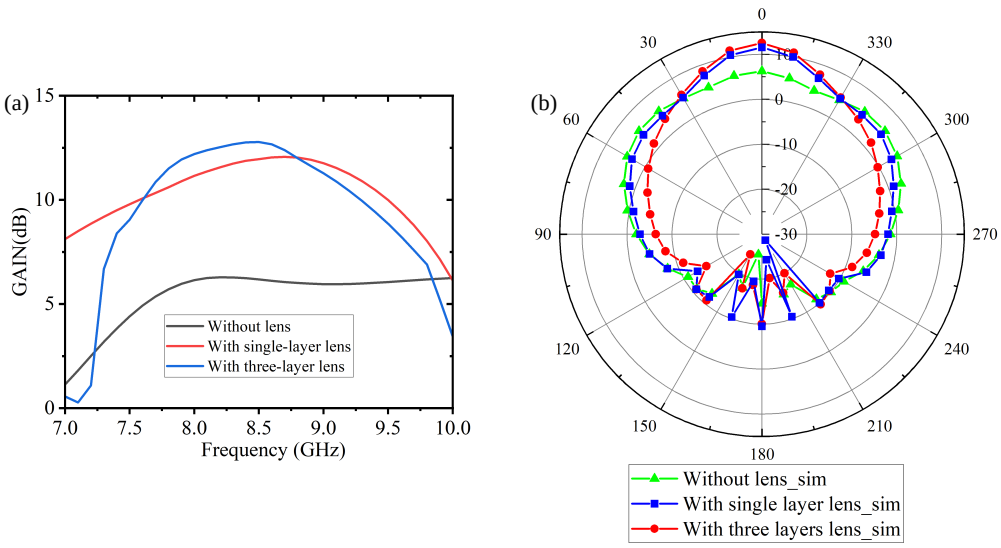

FIGURE 16. Comparison of gain and direction of antenna at 8.2 GHz, (a) gain comparison of feed antenna and metamaterial antenna, (b) direction comparison of feed antenna and metamaterial antenna.

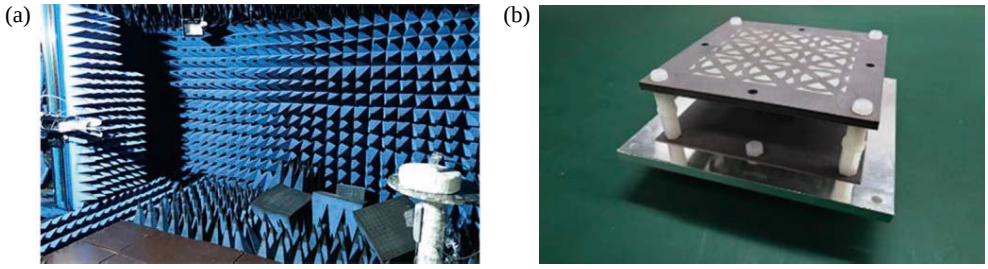

FIGURE 17. Test environment and antenna sample figure, (a) test environment, (b) antenna sample.

TABLE 2. Structural parameters of the feed antenna.

Parameter	Value (mm)	Parameter	Value (mm)	Parameter	Value (mm)	Parameter	Value (mm)
h_1	1.5	h_2	3	h_3	0.5	h_c	3
h_g	4	w_s	18	w_c	4.3	w_p	6
w_g	95.8	w_d	75.8	w_f	1.5	l_s	18
l_c	12.5	l_p	6	l_g	95.8	l_d	75.8
l_f	15.5	d_{x1}	38.9	d_{x2}	43.6	d_{y1}	35.7
d_{y2}	43.6	/	/	/	/	/	/

before and after loading, the maximum gain increased from 6.55 dBi to 12.06 dBi while maintaining a 3 dB gain bandwidth from 7.26 GHz to 9.66 GHz, with a relative gain bandwidth of 28.36%. The radiation pattern comparison shows a noticeable improvement in directivity. However, there is still room for further improvement in the antenna's radiation performance. Therefore, based on previous analysis, a three layers DB-NZRI FSS was created by unit 1, unit 2, and unit 3. By loading the three layers DB-NZRI FSS with different zero refractive index frequency points, the gain of antenna can be further improved while maintaining broadband.

After loading the three layers DB-NZRI FSS, the antenna's maximum gain increased from 6.74 dBi to 12.77 dBi with 3 dB bandwidth of 20.70% (from 7.58 GHz to 9.33 GHz). At 8.2 GHz, the directionality of the antenna has been significantly improved. In summary, the designed DB-NZRI FSS demonstrates excellent electromagnetic wave focusing performance and can effectively enhance the antenna gain.

3.2. The Experiment Verification of High-Gain Antenna Based on DB-NZRI FSS

Following the theoretical guidance, we constructed a physical model and tested its gain performance. The sample and test

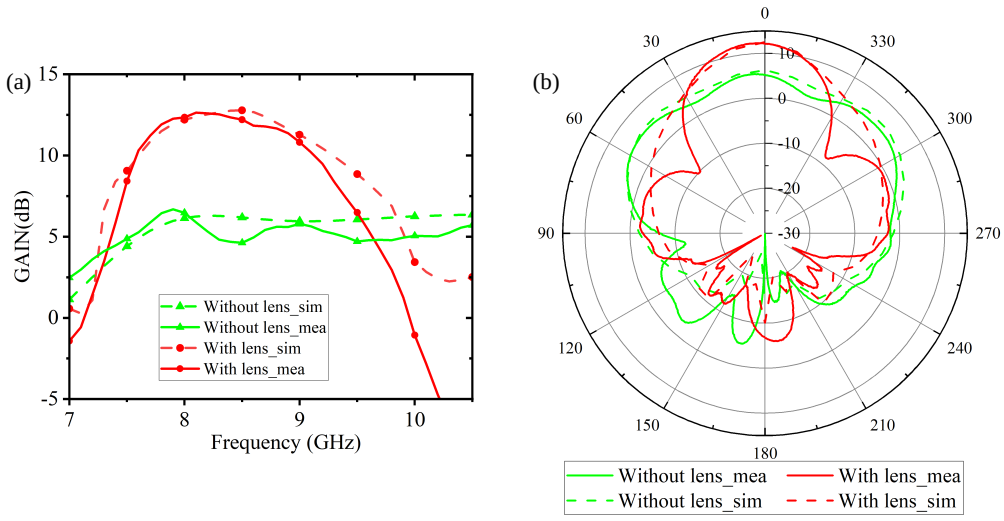

FIGURE 18. Comparison of actual antenna gain, (a) wideband gain enhancement, (b) gain enhancement at 8.2 GHz.

TABLE 3. Comparison of the proposed work with reference antennas.

Reference	Relative bandwidth (%)	Maximum gain (dBi)	Frequency (GHz)
[57]	14	14.5	7.7
[58]	3.85	3.48	5.2
[59]	4.7 and 3	12.3 and 14.2	43 and 43
[60]	8.6	12.31	7.45
This work	19.35	12.64	7.56–9.18

environment figures are shown in Fig. 17, and the test results are shown in Fig. 18. The antenna achieves a maximum gain of 12.64 dBi. At 8.2 GHz, the main lobe of the beam is controlled within $\pm 30°$. It was concluded after the experiment that the errors existing between the test data and simulation data were influenced by the experimental environment and processing errors. In summary, the test results matched the simulation results well. The proposed antenna features a wide bandwidth, high gain, and high directivity.

4. CONCLUSION

The metamaterial antenna that we proposed is compared with published works, and the comparison results are shown in Table 3. The proposed antenna has the advantage of dual frequency zero refractive index based on zero magnetic permeability, while achieving higher gain and wider 3 dB gain bandwidth.

This article proposes a broadband high gain antenna based on near zero refractive index materials designed using deep learning. It achieves a maximum gain of 12.64 dBi and a relative bandwidth of 19.35%, with good directivity. The proposed deep learning design method can quickly determine the corresponding structural parameters of the required S_{11} curve, thereby significantly accelerating the antenna design process.

ACKNOWLEDGEMENT

This work was supported by the National Key Research and Development Program of China (No. 2023YFB3811503), the National Natural Science Foundation of China (No. 62071423, No. 62288101), the Top-Notch Young Talent of China, the Natural Science Foundation of Zhejiang Province (No. LR23F010004, No. LZ24A050002), the Top-Notch Young Talent of Zhejiang Province, and the Key Research and Development Program of Zhejiang Province (No. 2024C01160), the Key Research and Development Program of Shaanxi (No. 2021TD-07), the Fundamental Research Funds for the Central Universities (No. 226-2024-00125), the Fundamental Research Funds for the Central Universities and the Innovation Fund of Xidian University (No. XJSJ24094, No. 20103224952 and No. XJSJ23016).

REFERENCES

[1] Chen, H., L. Ran, J. Huangfu, X. Zhang, K. Chen, T. M. Grzegorczyk, and J. A. Kong, "Left-handed materials composed of only S-shaped resonators," *Physical Review. E, Statistical, Nonlinear, and Soft Matter Physics*, Vol. 70, No. 5, Pt 2, 057605, Nov. 2004.

[2] Xi, S., H. Chen, T. Jiang, L. Ran, J. Huangfu, B.-I. Wu, J. A. Kong, and M. Chen, "Experimental verification of reversed Cherenkov radiation in left-handed metamaterial," *Phys. Rev. Lett.*, Vol. 103, 194801, Nov. 2009.

[3] Cai, T., S. Tang, B. Zheng, G. Wang, W. Ji, C. Qian, Z. Wang, E. Li, and H. Chen, "Ultrawideband chromatic aberration-free meta-mirrors," *Advanced Photonics*, Vol. 3, No. 1, 016001, 2021.

[4] Qian, C., X. Lin, Y. Yang, X. Xiong, H. Wang, E. Li, I. Kaminer, B. Zhang, and H. Chen, "Experimental observation of superscattering," *Physical Review Letters*, Vol. 122, No. 6, 063901, Feb. 2019.

[5] Valentine, J., J. Li, T. Zentgraf, G. Bartal, and X. Zhang, "An optical cloak made of dielectrics," *Nature Materials*, Vol. 8, No. 7, 568–571, 2009.

[6] Chen, H., B.-I. Wu, B. Zhang, and J. A. Kong, "Electromagnetic wave interactions with a metamaterial cloak," *Physical Review Letters*, Vol. 99, No. 6, 063903, Aug. 2007.

[7] Qian, C., B. Zheng, Y. Shen, L. Jing, E. Li, L. Shen, and H. Chen, "Deep-learning-enabled self-adaptive microwave cloak without human intervention," *Nature Photonics*, Vol. 14, No. 6, 383–390, 2020.

[8] Chen, H., B. Zheng, L. Shen, H. Wang, X. Zhang, N. I. Zheludev, and B. Zhang, "Ray-optics cloaking devices for large objects in incoherent natural light," *Nature Communications*, Vol. 4, No. 1, 2652, 2013.

[9] Yang, Y., L. Jing, B. Zheng, R. Hao, W. Yin, E. Li, C. M. Soukoulis, and H. Chen, "Full-polarization 3D metasurface cloak with preserved amplitude and phase," *Advanced Materials*, Vol. 28, No. 32, 6866–6871, 2016.

[10] Qian, C., Y. Jia, Z. Wang, J. Chen, P. Lin, X. Zhu, E. Li, and H. Chen, "Autonomous aeroamphibious invisibility cloak with stochastic-evolution learning," *Advanced Photonics*, Vol. 6, No. 1, 016001, 2024.

[11] Zheng, B., H. Lu, C. Qian, D. Ye, Y. Luo, and H. Chen, "Revealing the transformation invariance of full-parameter omnidirectional invisibility cloaks," *Electromagnetic Science*, Vol. 1, No. 2, 1–7, 2023.

[12] Cai, T., B. Zheng, J. Lou, L. Shen, Y. Yang, S. Tang, E. Li, C. Qian, and H. Chen, "Experimental realization of a superdispersion-enabled ultrabroadband terahertz cloak," *Advanced Materials*, Vol. 34, No. 38, 2205053, 2022.

[13] Huang, H., C. Guan, B. Zheng, X. Li, X. Cui, J. Liang, W. Jiang, H. Chen, and T. Cai, "Multiplexing meta-illusion with high correlation in both near- and far-field region," *Laser & Photonics Reviews*, Vol. 18, No. 11, 2400517, 2024.

[14] Yang, Y., Z. Gao, H. Xue, L. Zhang, M. He, Z. Yang, R. Singh, Y. Chong, B. Zhang, and H. Chen, "Realization of a three-dimensional photonic topological insulator," *Nature*, Vol. 565, No. 7741, 622–626, 2019.

[15] Ni, C., Z. Yu, L. Zhang, and Z. Zhang, "A wide-band circularly polarized and beam deflection antenna based on two metasurfaces," *IEEE Antennas and Wireless Propagation Letters*, Vol. 22, No. 12, 2861–2865, 2023.

[16] Yue, H., L. Chen, Y. Yang, L. He, and X. Shi, "Design and implementation of a dual frequency and bidirectional phase gradient metasurface for beam convergence," *IEEE Antennas and Wireless Propagation Letters*, Vol. 18, No. 1, 54–58, 2019.

[17] Liang, J.-J., G.-L. Huang, J.-N. Zhao, Z.-J. Gao, and T. Yuan, "Wideband phase-gradient metasurface antenna with focused beams," *IEEE Access*, Vol. 7, 20 767–20 772, 2019.

[18] Wang, W. and Y. Zheng, "Wideband gain enhancement of high-isolation Fabry-Pérot antenna array with tandem circular parasitic patches and radial gradient PRS," *IEEE Transactions on Antennas and Propagation*, Vol. 69, No. 11, 7959–7964, 2021.

[19] Moghadas, H., M. Daneshmand, and P. Mousavi, "Single-layer partially reflective surface for an orthogonally-polarised dual-band high-gain resonant cavity antenna," *IET Microwaves, Antennas & Propagation*, Vol. 7, No. 8, 656–662, 2013.

[20] Melouki, N., A. Hocini, and T. A. Denidni, "High-gain and wideband Fabry-Perot resonator antenna based on a pixelated single PRS layer for Ku-band applications," in *2022 IEEE International Symposium on Antennas and Propagation and USNC-URSI Radio Science Meeting (AP-S/URSI)*, 988–989, Denver, CO, USA, 2022.

[21] Lv, Y.-H., X. Ding, and B.-Z. Wang, "Dual-wideband high-gain Fabry-Perot cavity antenna," *IEEE Access*, Vol. 8, 4754–4760, 2019.

[22] Zhang, K., Y. Wang, Y. Yuan, and S. N. Burokur, "A review of orbital angular momentum vortex beams generation: From traditional methods to metasurfaces," *Applied Sciences*, Vol. 10, No. 3, 1015, 2020.

[23] Liu, B., Y. He, S.-W. Wong, and Y. Li, "Multifunctional vortex beam generation by a dynamic reflective metasurface," *Advanced Optical Materials*, Vol. 9, No. 4, 2001689, 2021.

[24] Li, J.-S. and L.-N. Zhang, "Simple terahertz vortex beam generator based on reflective metasurfaces," *Optics Express*, Vol. 28, No. 24, 36 403–36 412, 2020.

[25] Zhang, J., L. Han, X. Chen, R. Yang, and W. Zhang, "Multibeam patch antenna based on metasurface," *IEEE Access*, Vol. 8, 37 281–37 286, 2019.

[26] Stefanini, L., A. Rech, D. Ramaccia, S. Tomasin, A. Toscano, F. Moretto, and F. Bilotti, "Multibeam scanning antenna system based on beamforming metasurface for fast 5G NR initial access," *IEEE Access*, Vol. 10, 65 982–65 995, 2022.

[27] Li, W., T. Qiu, J. Wang, L. Zheng, Y. Jing, Y. Jia, H. Wang, Y. Han, and S. Qu, "Programmable coding metasurface reflector for reconfigurable multibeam antenna application," *IEEE Transactions on Antennas and Propagation*, Vol. 69, No. 1, 296–301, 2021.

[28] Wen, Y., P.-Y. Qin, S. Maci, and Y. J. Guo, "Low-profile multibeam antenna based on modulated metasurface," *IEEE Transactions on Antennas and Propagation*, Vol. 71, No. 8, 6568–6578, 2023.

[29] Costa, F., A. Monorchio, and G. Manara, "An overview of equivalent circuit modeling techniques of frequency selective surfaces and metasurfaces," *Applied Computational Electromagnetics Society Journal (ACES)*, Vol. 29, No. 12, 960–976, 2014.

[30] Dadgarpour, A., B. Zarghooni, B. S. Virdee, and T. A. Denidni, "Beam-deflection using gradient refractive-index media for 60-GHz end-fire antenna," *IEEE Transactions on Antennas and Propagation*, Vol. 63, No. 8, 3768–3774, 2015.

[31] Ma, C., Z. Wang, H. Zhang, F. Yang, J. Chen, Q. Ren, Y. Ma, and N. Wang, "Inverse design of electromagnetic metamaterials: From iterative to deep learning-based methods," *Journal of Micromechanics and Microengineering*, Vol. 34, No. 5, 053001, 2024.

[32] You, X. and F. H. Lin, "Energy efficient design of low-profile wideband microstrip patch antennas using deep learning," in *2023 International Conference on Microwave and Millimeter Wave Technology (ICMMT)*, 1–3, Qingdao, China, 2023.

[33] Hou, Z., T. Tang, J. Shen, C. Li, and F. Li, "Prediction network of metamaterial with split ring resonator based on deep learning," *Nanoscale Research Letters*, Vol. 15, 1–8, 2020.

[34] Wang, J., R. Xi, T. Cai, H. Lu, R. Zhu, B. Zheng, and H. Chen, "Deep neural network with data cropping algorithm for absorptive frequency-selective transmission metasurface," *Advanced Optical Materials*, Vol. 10, No. 13, 2200178, 2022.

[35] Qian, C., X. Lin, X. Lin, J. Xu, Y. Sun, E. Li, B. Zhang, and H. Chen, "Performing optical logic operations by a diffractive

neural network," *Light: Science & Applications*, Vol. 9, No. 1, 59, 2020.

[36] Liang, M., Z. Li, T. Chen, and J. Zeng, "Integrative data analysis of multi-platform cancer data with a multimodal deep learning approach," *IEEE/ACM Transactions on Computational Biology and Bioinformatics*, Vol. 12, No. 4, 928–937, 2015.

[37] Bai, X., X. Wang, X. Liu, Q. Liu, J. Song, N. Sebe, and B. Kim, "Explainable deep learning for efficient and robust pattern recognition: A survey of recent developments," *Pattern Recognition*, Vol. 120, 108102, 2021.

[38] Cao, K., C. Jin, B. Zhang, Q. Lv, and F. Lu, "Beam stabilization of deformed conformal array antenna based on physical-method-driven deep learning," *IEEE Transactions on Antennas and Propagation*, Vol. 71, No. 5, 4115–4127, 2023.

[39] Lu, H., J. Zhao, B. Zheng, C. Qian, T. Cai, E. Li, and H. Chen, "Eye accommodation-inspired neuro-metasurface focusing," *Nature Communications*, Vol. 14, No. 1, 3301, 2023.

[40] Emmert-Streib, F., Z. Yang, H. Feng, S. Tripathi, and M. Dehmer, "An introductory review of deep learning for prediction models with big data," *Frontiers in Artificial Intelligence*, Vol. 3, 4, 2020.

[41] Johnston, R. L., "Evolving better nanoparticles: Genetic algorithms for optimising cluster geometries," *Dalton Transactions*, Vol. 22, No. 22, 4193–4207, 2003.

[42] Giles, M. B. and N. A. Pierce, "An introduction to the adjoint approach to design," *Flow, Turbulence and Combustion*, Vol. 65, 393–415, 2000.

[43] Lee, Y. E., O. D. Miller, M. T. H. Reid, S. G. Johnson, and N. X. Fang, "Computational inverse design of non-intuitive illumination patterns to maximize optical force or torque," *Optics Express*, Vol. 25, No. 6, 6757–6766, 2017.

[44] Ma, W., F. Cheng, Y. Xu, Q. Wen, and Y. Liu, "Probabilistic representation and inverse design of metamaterials based on a deep generative model with semi-supervised learning strategy," *Advanced Materials*, Vol. 31, No. 35, 1901111, 2019.

[45] Noh, J., Y.-H. Nam, S. So, C. Lee, S.-G. Lee, Y. Kim, T.-H. Kim, J.-H. Lee, and J. Rho, "Design of a transmissive metasurface antenna using deep neural networks," *Opt. Mater. Express*, Vol. 11, 2310–2317, 2021.

[46] Scardapane, S., S. V. Vaerenbergh, A. Hussain, and A. Uncini, "Complex-valued neural networks with nonparametric activation functions," *IEEE Transactions on Emerging Topics in Computational Intelligence*, Vol. 4, No. 2, 140–150, 2020.

[47] Guo, Y., J. Zhao, and X. Zhao, "A novel high-gain omnidirectional antenna using near-zero-index metamaterials," *Microwave and Optical Technology Letters*, Vol. 64, No. 7, 1280–1287, 2022.

[48] Konstantinidis, K. and A. P. Feresidis, "Broadband near-zero index metamaterials," *Journal of Optics*, Vol. 17, No. 10, 105104, 2015.

[49] Zhu, S., H. Liu, P. Wen, L. Du, and J. Zhou, "A miniaturized and high gain double-slot Vivaldi antenna using wideband index-near-zero metasurface," *IEEE Access*, Vol. 6, 72 015–72 024, 2018.

[50] Trentini, G. V., "Partially reflecting sheet arrays," *IRE Transactions on Antennas and Propagation*, Vol. 4, No. 4, 666–671, 1956.

[51] Pang, K., M. Z. Alam, Y. Zhou, C. Liu, O. Reshef, K. Manukyan, M. Voegtle, A. Pennathur, C. Tseng, X. Su, *et al.*, "Adiabatic frequency conversion using a time-varying epsilon-near-zero metasurface," *Nano Letters*, Vol. 21, No. 14, 5907–5913, 2021.

[52] Zhou, Y., M. Z. Alam, M. Karimi, J. Upham, O. Reshef, C. Liu, A. E. Willner, and R. W. Boyd, "Broadband frequency translation through time refraction in an epsilon-near-zero material," *Nature Communications*, Vol. 11, No. 1, 2180, 2020.

[53] Wang, Z., P. Zhou, and G. Zheng, "Electrically switchable highly efficient epsilon-near-zero metasurfaces absorber with broadband response," *Results in Physics*, Vol. 14, 102376, 2019.

[54] Szabó, Z., G.-H. Park, R. Hedge, and E.-P. Li, "A unique extraction of metamaterial parameters based on Kramers-Kronig relationship," *IEEE Transactions on Microwave Theory and Techniques*, Vol. 58, No. 10, 2646–2653, 2010.

[55] Liu, S. and J. Wu, *Digital Signal Processing*, 3rd ed., Xi'an Electronic and Science Technology University Press, 2015.

[56] Liu, Y., S. Chen, Y. Ren, J. Cheng, and Q. H. Liu, "A broadband proximity-coupled dual-polarized microstrip antenna with L-shape backed cavity for X-band applications," *AEU — International Journal of Electronics and Communications*, Vol. 69, No. 9, 1226–1232, 2015.

[57] Majumder, B., K. Kandasamy, and K. P. Ray, "A zero index based meta-lens loaded wideband directive antenna combined with reactive impedance surface," *IEEE Access*, Vol. 6, 28 746–28 754, 2018.

[58] Guo, Y., J. Zhao, and X. Zhao, "A novel high-gain omnidirectional antenna using near-zero-index metamaterials," *Microwave and Optical Technology Letters*, Vol. 64, No. 7, 1280–1287, 2022.

[59] Bouzouad, M., S. M. Chaker, D. Bensafielddine, and E. M. Laamari, "Gain enhancement with near-zero-index metamaterial superstrate," *Applied Physics A*, Vol. 121, No. 3, 1075–1080, 2015.

[60] Rajanna, P. K. T., K. Rudramuni, and K. Kandasamy, "A high-gain circularly polarized antenna using zero-index metamaterial," *IEEE Antennas and Wireless Propagation Letters*, Vol. 18, No. 6, 1129–1133, 2019.